Chem Catalysis

CellPress

Article

First-principle-data-integrated machine-learning approach for high-throughput searching of ternary electrocatalyst toward oxygen reduction reaction

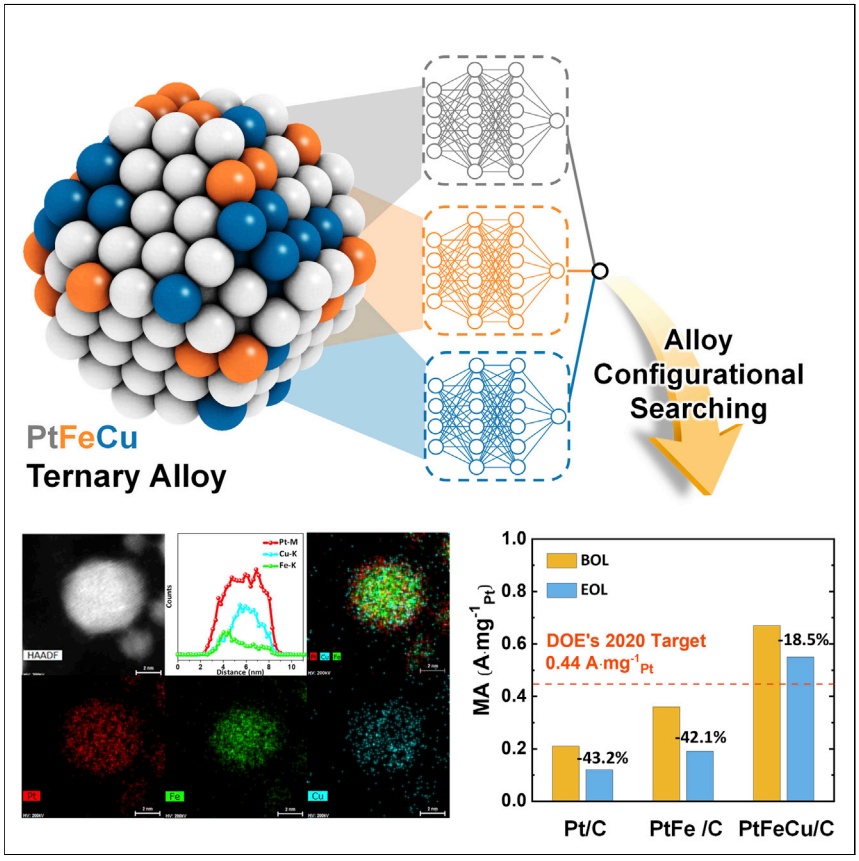

To efficiently design the Pt-based alloy nanocatalysts for oxygen reduction reaction, we utilized first-principle data integrated with machine learning to search for PtFeCu configurational spaces. We identified the promising candidates and revealed the atomic-level understanding via first-principle calculations. Cu atomic distribution remarkably modulated surface strain energies and segregation of the alloying components toward better oxygen reduction reaction performance. Tuning of Cu contents led to the high electrochemical performance of PtFeCu nanocatalysts, which was successfully validated by experiments.

Hoje Chun, Eunjik Lee, Kyungju Nam, Ji-Hoon Jang, Woomin Kyoung, Seung Hyo Noh, Byungchan Han

singsingi@hyundai.com (S.H.N.)
bchan@yonsei.ac.kr (B.H.)

Highlights

First-principle establishment of catalytic property data for ternary nanoparticles

Parametrization of atomistic interaction into neural network potentials

A striking consistency between computational prediction and experimental validation

Exceptional catalytic mass activity of PtFeCu 3-fold higher than that of Pt/C

Chun et al., Chem Catalysis 1, 855–869
September 16, 2021
https://doi.org/10.1016/j.checat.2021.06.001

Chem Catalysis

CellPress

Article

First-principle-data-integrated machine-learning approach for high-throughput searching of ternary electrocatalyst toward oxygen reduction reaction

Hoje Chun,[1,4] Eunjik Lee,[2,3,4] Kyungju Nam,[3] Ji-Hoon Jang,[3] Woomin Kyoung,[3] Seung Hyo Noh,[3,*] and Byungchan Han[1,5,*]

SUMMARY

Platinum (Pt) alloys are expected to overcome long-standing issues of Pt/C electrocatalysts for oxygen reduction reaction (ORR). Entangled with serious uncertainty in configurational and compositional information, the design of a promising multi-component electrocatalyst, however, has been delayed. Here, we demonstrate that a first-principle database-driven machine-learning approach is extremely useful for the purpose via exploring materials beyond the regime of pure quantum mechanical calculations. Guided by a computational ternary phase diagram we indeed experimentally synthesized a PtFeCu nanocatalyst with 2 g per batch capacity and measured its catalytic performance for ORR. Both our computation and experiment consistently demonstrate that PtFeCu is highly active due to the atomic distribution of Cu leading to beneficial modulation of surface strain and segregation. Strikingly, $PtFe_{high}Cu_{low}$ (776 $\mu A\ cm^{-2}_{Pt}$ and 0.67 $A\ mg^{-1}_{Pt}$) exhibits not only 3-fold better specific and mass activities than Pt/C but also little performance degradation over the accelerated stress test.

INTRODUCTION

Proton exchange membrane (PEM) fuel cells are promising due to their direct conversion of chemical energy into electric power.[1,2] They are not only more efficient but also more environmentally friendly than combustion engines. It is not surprising that advanced countries over the world adopted PEM fuel cells as renewable power sources of electric locomotives.[3]

In practice, however, the efficiency and life span of PEM fuel cells are much lower than theoretical prediction, in which nanocatalysts involved with kinetic reaction are located at the center of the problems. The high material cost, substantial overpotential, and instability in cycling operation of Pt-based nanocatalysts are the main causes. Especially, oxygen reduction reaction (ORR), one of the key electrochemical reactions, is kinetically very sluggish with Pt nanoparticles in the cathode and even the noble materials suffer serious structural degradation via mutual agglomeration or dissolution into acidic aqueous solution.[4,5]

Over the last few decades, considerable amounts of concerted works have been conducted to develop active and durable electrocatalysts, but unfortunately no commercial-grade alternative to costly Pt metal was deployed.[5,6] There is a consensus that a pure Pt nanoparticle cannot meet the desired catalytic performances of activity and durability for ORR in PEM fuel cell operation. Thus, various

The bigger picture

One of the challenging issues in nanocatalyst design for catalysis applications is to introduce the atomic-level functionalities of nanoparticles, determining the activity and stability. Multi-component systems can be promising, but the enormous configurational degrees of freedom and optimization routes for a target reaction remained unsolved. We demonstrate the combination of a machine-learning approach and experimental tests of PtFeCu nanoparticles for oxygen reduction reaction. Promising candidates were efficiently screened theoretically and successfully validated by the experiments. Both our computational and experimental outcomes indicate that the highly active electrocatalytic performance of PtFeCu originates from Cu atomic distribution. Our study suggests that first-principle calculations combined with machine-learning technology can be a promising approach in design of nanocatalysts to reduce the gap between the simulations and experiments.

nanoscale alloy particles have been proposed,[7,8] expecting a synergic effect from the components. Several binary Pt alloys (PtM with M = Cu, Fe, Co, Ni, Y, etc.) have been investigated extensively for ORR catalysis guided by theoretical and computational models claiming that the activity can be improved substantially by tuning the binding energies of reactants and intermediates in the rate-determining steps.[9–13] Indeed, the ordered *fct*-PtFe nanoparticles had a better ORR performance than pure Pt due to the weaker OH binding energy on its surface and compressive strain to Pt by the smaller Fe.[10]

Another interesting example is the so-called core-shell nanoparticles of Pt (shell) with 3d transition metals (core). In the system, ORR is catalyzed by the surface Pt, while the cheaper and smaller transition metals located at the core induce compressive strain to enhance the activity of the Pt. The core-shell nanoparticles can be also more resistive against dissolution due to the protective Pt atomic shells. Likewise, both $PtCu_3$ and PtCo exhibited outstanding catalytic performance toward ORR.[11,14] Despite the promising reports, binary nanocatalysts of Pt-M still were observed to undergo structural degradation during long-term electrochemical cyclings.[15,16] Surface segregation of core elements followed by electrochemical dissolution induced by oxidative adsorbates was proposed as its major mechanism.[17] This clearly indicates that two-component alloy nanocatalysts may not be sufficient to ensure both catalytic activity and durability in the practical operation of PEM fuel cells.

Introducing a third component is an attractive strategy to further modulate the catalytic performance and stability of the ORR in acid media. Several studies have been reported in which Pt-based ternary nanoparticles were used for ORR catalysis.[18–21] Arumugam et al.[22] elucidated that Cu helps stabilize nanoscale PtFe intermetallic compounds by protecting the Fe from electrochemical dissolution. Also, it has been reported that the stoichiometric number of each component is important for achieving optimal oxygen binding energy for ORR catalytic activity.[23] A more recent combined computational and experimental study has indicated that the elemental distributions of Ni and Cu are important for the long-term stability of PtNiCu.[24] Likewise, ternary nanoparticles still can be promising electrocatalysts with superior activity and durability to binary nanoparticles.

Yet, there has been no extensive exploration of the configurational and compositional space in ternary alloys because the task is challenging irrespective of whether experimental or computational methods are used. In experiments, the formidably multi-dimensional variables for both the characterization of electrocatalytic performance and fabrication routes for ternary nanoparticles result in uncertainties concerning the accurate and comprehensive understanding of the catalytic properties. Computational approaches often have both significant uncertainties concerning the sizes and configurations of materials and computational costs that are increasing exponentially, even with the present-day supercomputing architectures.

It is noteworthy that the state-of-the-art machine-learning technique has been used successfully to solve scientific problems, which has not been the case for conventional computational methodologies.[25–29] The key idea in the approach is to parametrize atomistic interaction energies into a neural network as a function of structural descriptors locally constructed by component species. Various efficient algorithms of the machine-learning technique, such as the high-dimensional neural network, Gaussian processing regression, and kernel ridge regression have been used to parametrize the atomic contribution of energy to the system.

[1]Department of Chemical and Biomolecular Engineering, Yonsei University, Seoul 03722, Republic of Korea

[2]Fuel Cell Laboratory, Korea Institute of Energy Research, 152, Gajeong-ro, Yuseong-gu, Daejeon 34129, Republic of Korea

[3]Institute of Fundamental and Advanced Technology, R&D Division, Hyundai Motor Company, Uiwang 16082, Republic of Korea

[4]These authors contributed equally

[5]Lead contact

*Correspondence: singsingi@hyundai.com (S.H.N.), bchan@yonsei.ac.kr (B.H.)

https://doi.org/10.1016/j.checat.2021.06.001

The integration of first-principle calculations and machine-learning algorithms is a very attractive approach to deal with the long-standing problems associated with conventional computational methods (materials gaps and costly calculations) in that the neural network potential (NNP) can be established successfully through rational selection and an extensive train of samples from an accurate database. For example, the Behler group[30–32] applied the NNP in a wide range of fields, from surface catalysis to metal organic frameworks, and Artrith and Kolpak[33] demonstrated the NNP with bimetallic AuCu nanocatalysts for the reduction of CO_2. In our previous study,[34] it was shown that the NNP can facilitate the design of functional nanomaterials for ORR. However, the compositional variations were limited, and experimental validation was not done. Note that experimental validations of predictions from state-of-the-art approaches are still insecure.

Herein, we extensively utilized the first-principle density functional theory (DFT) calculations interlocked with the machine learning technique for PtFeCu nanoparticles as large as 2 nm. Using DFT calculations, we established an accurate database for the catalytic properties of the ternary PtFeCu models for ORR, which were analyzed using a deep learning algorithm to parametrize the atomistic interaction potentials. Our approach mapped a ternary phase diagram from a high-throughput screen of 396,862 structures, which were validated consistently through experimental synthesis via a simple and fast sonication method that yielded products approaching a commercial-grade product, while excelling the lab-scale products (mg). Using four representative ternary PtFeCu nanoparticles with varying compositions, we extensively validated the computational predictions by experimental tests for ORR activity and stability. We identified the most promising ORR electrocatalyst structure of PtFeCu nanoparticles and its underlying mechanism via electronic structures and the surface strain distribution to propose a key design principle. Our proposed ORR electrocatalyst, $PtFe_{high}Cu_{low}$, surpassed the 2020 US Department of Energy's (DOE's) target for both mass activity and stability.

RESULTS AND DISCUSSION

NNP construction

To efficiently obtain the NNPs for the ternary PtFeCu nanoparticles, we decoupled the shape effects (morphology and size) and alloy effects (composition and configuration) as shown in Figure 1. The dataset was constructed to simulate the configurational space of the PtFeCu nanoparticles. Atomic environments for large nanoparticles were duplicated, leading to the transferability of the NNP, but they were exposed to significantly different local environments for smaller nanoparticles. This can be regulated by changing the cutoff radius considering the local atomic environment, but a small cutoff radius leads to a lack of information, while a large cutoff radius increases the computational cost by a tremendous amount. Thus, the cutoff radius was set as 5 Å to ensure the atomic environment of the nearest neighbor atoms (Figure S1). Consequentially, a total of 44,884 atomic local environments were prepared with PtFeCu compositional and configurational space, and they were split randomly into a training set and a test set. Our NNP was trained successfully, such that the root-mean-square error (RMSE) of the test set, which also contained structures different from the training structures (larger-sized nanoparticles with random compositions), was 10.34 meV $atom^{-1}$ (Figure S4). It was shown that the shape and alloy effects were dependent on the cutoff radius (details are included in the supplemental information).

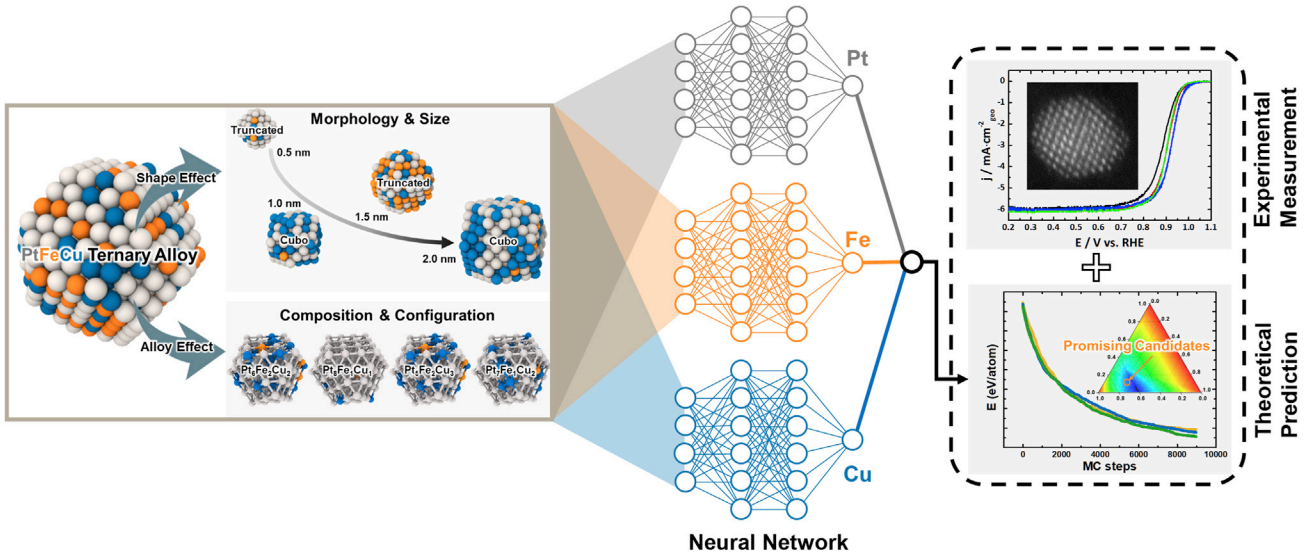

Figure 1. Schematic diagram of ternary alloy configuration search and theoretical predictions and experimental validation for ORR

Investigation of the stable configuration of ternary alloys

Using parametrized NNPs, we explored 2.0 nm ternary PtFeCu nanoparticles of a truncated octahedron in the composition range of $0.6 < Pt < 1$ atomic fraction. The lower limit of the Pt composition was set since it is a minimal Pt-skinned PtFeCu nanoparticle. Among the screened nanoparticles, we identified the most thermodynamically stable configurations with varying alloying compositions by Monte Carlo (MC) simulations along the Pt composition line, as shown in Figure 2. It clearly shows that each alloying element prefers to occupy a specific shell (Figures 2A–2C). Pt atoms tend to be in the outermost (first) shell, while the Fe atoms tend to be in the second shell, and the Cu atoms are dispersed somewhat randomly over the inner shells of the nanoparticles. The Pt in these ternary nanoparticles should be under compressive strain by the smaller Fe atom. Figures 2D–2F present the same trends as Figures 2A–2C. These results are consistent with the experimental observations of typical Pt-based alloy catalysts.[11,35]

From the configurational analysis, it is apparent that the amounts of Pt should be more than the ideal composition (0.6) to configure a Pt-skinned structure with a Fe-Cu core (Figure 2A). This implies that the ternary compounds have subtle interactions, which cannot be captured solely by the thermodynamic surface energy aspect, e.g., Pt has the lowest surface energy among the three elements. Furthermore, Fe is likely to be in the subshells, and Cu progressively occupies the core site as Pt composition decreases (Figures 2D–2F).

We mapped the ternary phase diagram using the DFT calculations of alloy PtFeCu nanoparticles, as shown in Figures 3A and 3B, in which the ground-state structures are identified with an energy convex hull in the composition range of $0.6 < Pt < 1.0$. The hull points appearing at Pt compositions greater than 0.8 mostly show the structures of the Pt-skinned shell. Below the Pt composition of 0.8, Fe and Cu likely are co-distributed in the first shell. As shown in Figures 2D–2F, Cu is more likely to be in the first shell than Fe:Pt compositions, in which the compositions of Cu and Fe start to appear in the first shell are 0.80 and 0.73, respectively.

To foresee the catalytic performance of PtFeCu ternary nanoparticles for ORR, three different compositions were selected, i.e., $Pt_{0.82}Fe_{0.18}$ (PtFe), $Pt_{0.82}Fe_{0.12}Cu_{0.06}$

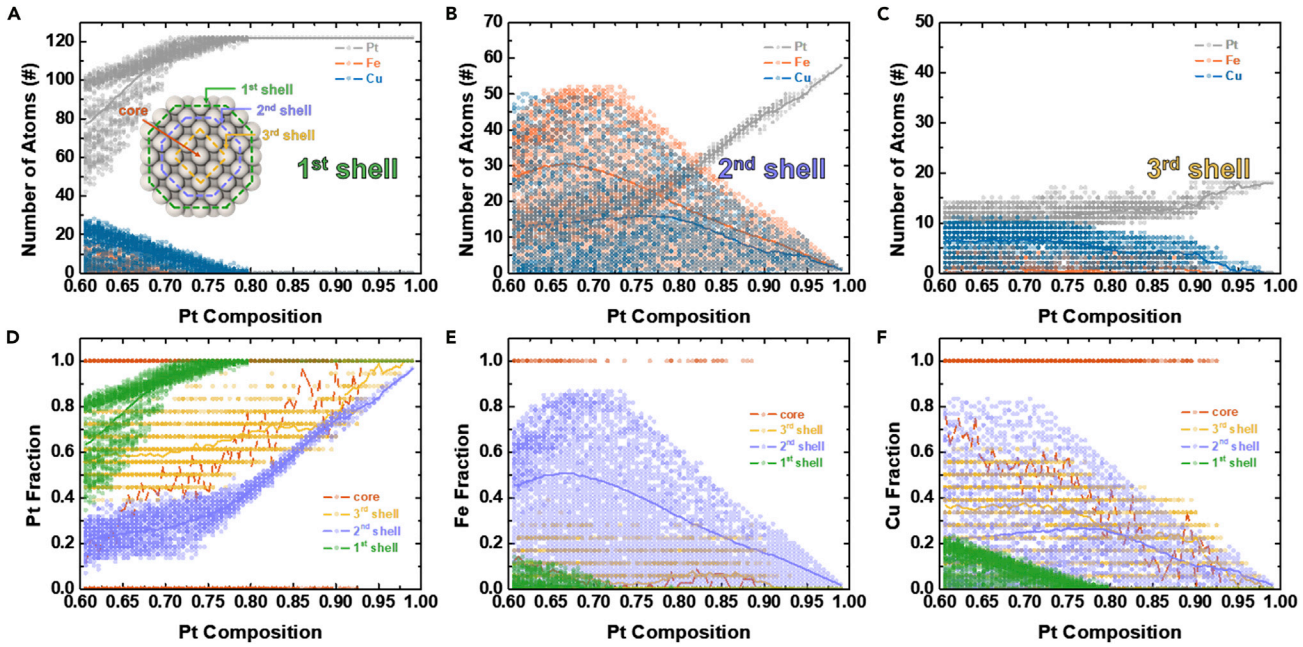

Figure 2. Configurational spaces of PtFeCu ternary nanoparticles of 2.0 nm size in the range of 0.6 < Pt < 1

Number of atoms in the (A) first shell, (B) second shell, and (C) third shell of the 2.0 nm truncated PtFeCu ternary nanoparticles. Atomic fraction of (D) Pt, (E) Fe, and (F) Cu in each shell of the 2.0 nm, truncated PtFeCu ternary nanoparticles.

($PtFe_{high}Cu_{low}$), and $Pt_{0.8}Fe_{0.08}Cu_{0.12}$ ($PtFe_{low}Cu_{high}$), as shown in Figure 3D, considering that the alloy nanoparticles should have the Pt-skinned structure and thermodynamically stable energy convex hull points. It is to be noted that the Cu compositions were restricted since the Cu tends to be located at the outermost shell as its content increases. Then, structures with the corresponding compositions were synthesized to cross-validate the computational predictions. Figure 3C shows the X-ray diffraction patterns of the PtFe and PtFeCu catalysts that were synthesized, along with the commercial Pt/C. The lattice symmetries of almost all the nanoparticles are the face-centered cubic symmetry, of which topologies are truncated octahedra (Figure S12).[36] In addition, phase separation was not observed in all of the regions. We also found that the (111) peak positions of PtFe and PtFeCu catalysts were shifted to higher angles than the peak position of Pt/C, which indicates that the relatively small-sized Fe and Cu atoms were incorporated into the Pt lattice, inducing the compressive strain.[37,38] Based on the Scherrer equation, the crystallite sizes of the samples were calculated as 2.1, 2.2, and 2.3 nm for $Pt_{0.83}Fe_{0.17}$ (PtFe), $Pt_{0.78}Fe_{0.15}Cu_{0.07}$ ($PtFe_{high}Cu_{low}$), and $Pt_{0.8}Fe_{0.09}Cu_{0.13}$ ($PtFe_{low}Cu_{high}$), respectively. As shown in Figure S8, the particle size and distribution were confirmed from low-magnified transmission electron microscopy (TEM) images. All samples show highly dispersed and uniform particle sizes (~3 nm) on the carbon support.

We performed STEM-EDS mapping and line profiles scanned with 0.08 nm of point resolution to investigate the compositional information of the PtFe and PtFeCu nanoparticles by analyzing the elemental distribution, as shown in Figures 3E and 3F. In the case of PtFe nanoparticles, we observed that the Fe-K signal existed in the core region, and the Pt-M signal existed throughout the entire nanoparticle. Based on the difference between the two profiles, it can be expected that the PtFe catalyst consists of approximately one or two layers of Pt shell (~0.3–0.5 nm) on the surface of the catalyst. Also, the PtFeCu catalyst had core-shell structure irrespective of its composition. It is expected

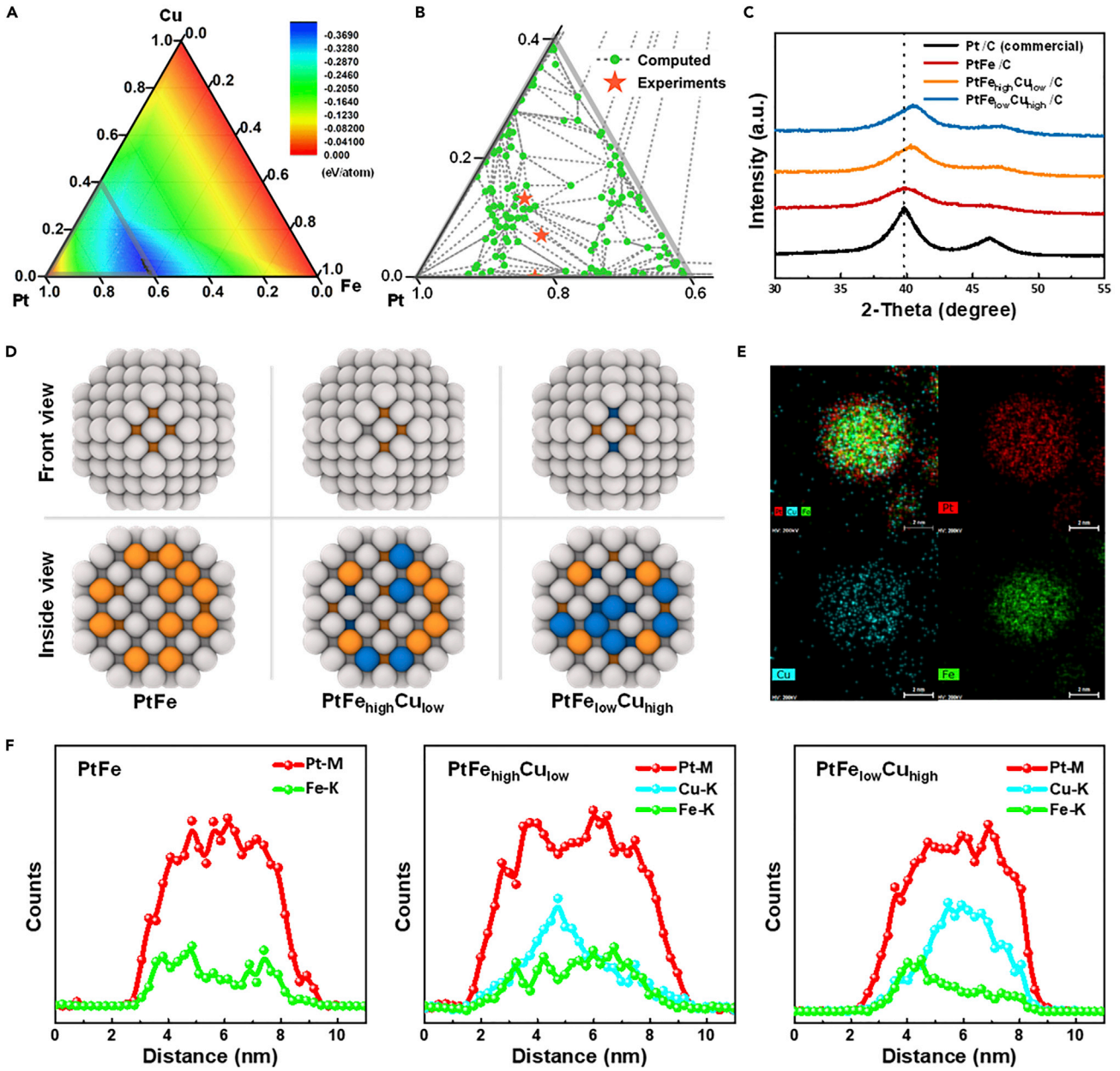

Figure 3. Thermodynamic ternary diagram and spectroscopic characterization Pt-based ternary nanoparticles

(A and B) (A) Ternary diagram and (B) the convex hull points of PtFeCu ternary nanoparticles (2.0 nm) in the range of 0.6 < Pt < 1. The orange stars are synthesized compositions.

(C and D) (C) XRD patterns and (D) structural information of representative compositions of PtFe and PtFeCu nanoparticles.

(E) Scanning transmission electron microscopy-energy dispersive X-ray spectroscopy (STEM-EDS) mapping.

(F) STEM-EDS line profiles.

The dotted line in (C) indicates the (111) peak of Pt (JCPDS no. 04-0802).

that the sequential acid treatment and heat treatment during the synthesis led to the formation of this core-shell structure.[35] In addition, we confirmed that more of the Cu atoms than the Fe atoms were distributed outside the NP (Figure 3E). The PtFeCu nanoparticles that were synthesized experimentally have similar structural conditions, such as particle size, compositions, and elemental distribution, i.e., they are consistent with the computational model systems.

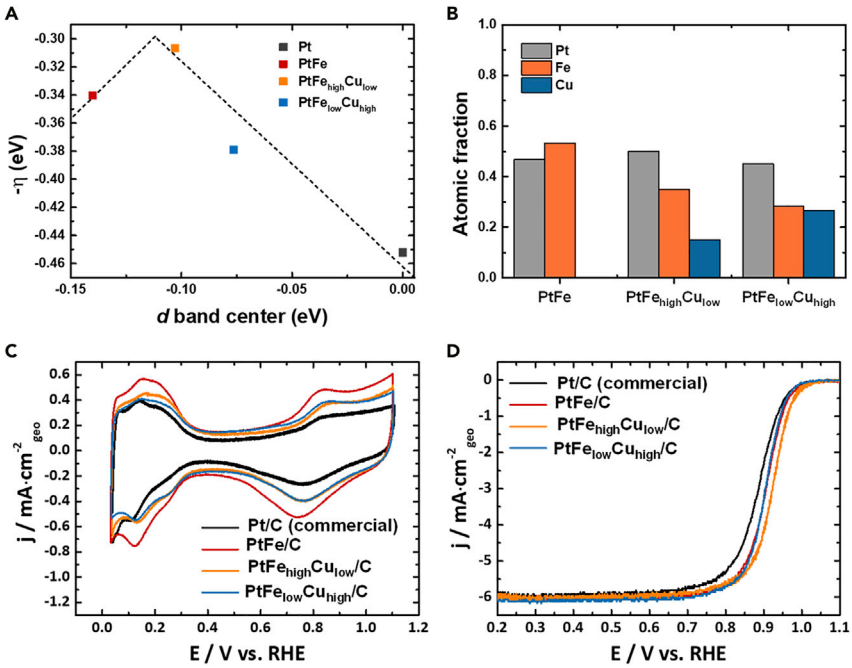

Figure 4. Theoretical predictions and electrochemical performance of pure (Pt), binary (PtFe), and ternary (PtFeCu) nanoparticles

(A) Calculated catalytic activity volcano for the ORR via *d* band center energy of Pt.

(B) Elemental distribution in the subshell (second shell) of 2.0 nm PtFe and PtFeCu nanoparticles.

(C and D) (C) CVs and (D) LSV curves for ORR.

Identification of a promising ORR electrocatalyst

Catalytic performance was evaluated by mapping the free energy diagram of ORR for four nanoparticles, i.e., Pt, PtFe, PtFe$_{high}$Cu$_{low}$, and PtFe$_{low}$Cu$_{high}$ (Figure S5). The performance was in the order of PtFe$_{high}$Cu$_{low}$ > PtFe > PtFe$_{low}$Cu$_{high}$ > Pt with overpotentials of 0.31, 0.33, 0.37, and 0.45 eV, respectively. The prediction was consistent with the *d* band center energy of Pt, as shown in Figure 4A. It is noteworthy that PtFe$_{high}$Cu$_{low}$ is at the top of the volcano among the nanoparticles due to the optimal binding energy of the oxygenate intermediates.

It has been reported[10] that the activity of Pt-based alloy nanocatalysts can be regulated by the strain field by mixing different sized elements in a nanoparticle. The key feature in this technology is to locate proper amounts of strain for the optimal binding energy. This is because strain energy regulates the *d* band center energy. Thus, the control of the spatial distribution of elements with different size is important for tuning the catalytic activity. As shown in Figure 4B, the elemental distributions in the second shell of the PtFe, PtFe$_{high}$Cu$_{low}$, and PtFe$_{low}$Cu$_{high}$ were computed. It is shown clearly that the compressive strain is linearly correlated with the amounts of Fe in the second shell. As the Cu loading increased, the amounts of Pt did not change significantly, while that of Fe decreased, which largely affects the level of compressive stain with smaller size of Fe than Pt. Consequentially, small amounts of Cu loading bring the *d* band center energy toward the optimal.

The electrocatalytic performance of our nanoparticles was determined with a typical three-electrode cell in an acid medium to validate the theoretical predictions. Figure 4C shows the cyclic voltammograms (CVs) of our samples in N_2-saturated

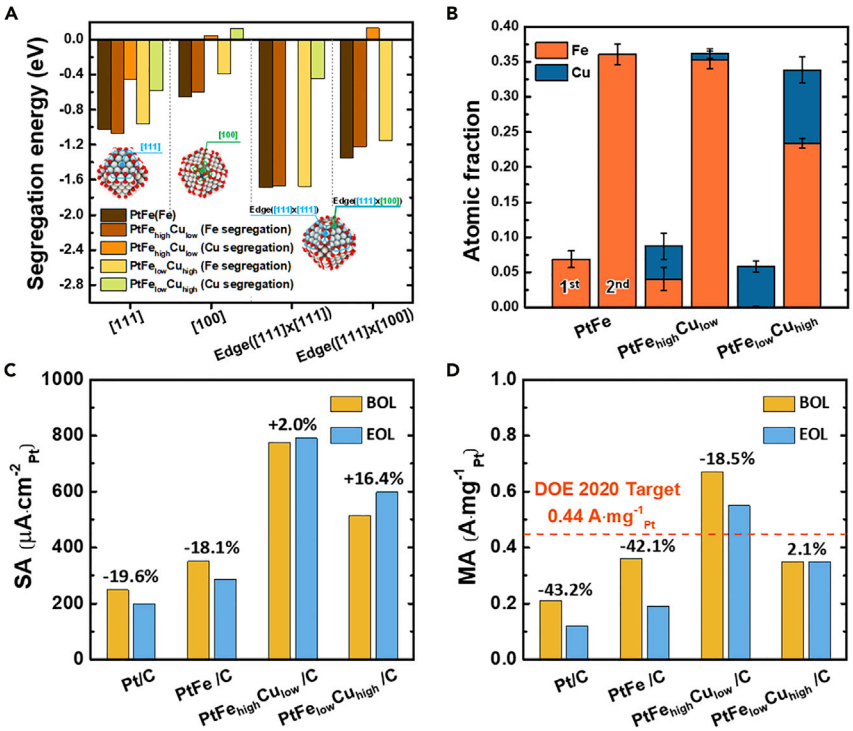

Figure 5. Electrochemical and chemical stabilities of pure (Pt), binary (PtFe), and ternary (PtFeCu) nanoparticles

(A) Surface segregation energy of alloy component predicted by DFT calculations. The segregation of Cu to edge([111] × [111]) sites in $PtFe_{high}Cu_{low}$ nanoparticle is not thermodynamically plausible.

(B) Atomic fraction of the first and second shell of the 3 nm nanoparticles with 807 atoms of PtFe, $PtFe_{high}Cu_{low}$, and $PtFe_{low}Cu_{high}$ for experimental composition (error bars represent standard deviation from the mean).

(C and D) (C) Specific activity and (D) mass activity at 0.9 V (versus RHE) before and after AST 30k.

0.1 M $HClO_4$ along with that of Pt/C. Interestingly, both $PtFe_{high}Cu_{low}$ and $PtFe_{low}Cu_{high}$ had Cu dissolution peaks at 0.7 V in the first cycle,[39] but the peaks disappeared immediately, which provided evidence of the de-alloying of the Cu from the outermost layer (Figure S9). This observation is consistent with our computational outcomes, i.e., that Cu tends to locate at the outermost layer of the nanoparticles as the Cu loading increases (Figure 2A). The electrochemical surface area (ECSA) of the samples was evaluated by integrating the electrical charges for the hydrogen desorption peak in the potential range of 0.03–0.4 V (versus reversible hydrogen electrode [RHE]).[40] The calculated ECSAs of the samples were 84.1 102.6, 86.7, and 67.4 $m^2\ g^{-1}_{Pt}$ for Pt/C, PtFe, $PtFe_{high}Cu_{low}$, and $PtFe_{low}Cu_{high}$, respectively (Figure S11).

The linear sweep voltammograms (LSVs) of the samples for ORR were recorded in O_2-saturated 0.1 M $HClO_4$ electrolyte with a rotating speed of 1,600 rpm. Compared with Pt/C, the PtFe and PtFeCu catalysts show both a higher onset potential and half-wave potential ($E_{1/2}$). Figures 5C and 5D show that the $PtFe_{high}Cu_{low}$ exhibits the highest specific (776 μA cm^{-2}_{Pt}) and mass (0.67 $m^2\ g^{-1}_{Pt}$) activities at 0.9 V, amounting to 3.1 and 3.2 times better than those of Pt/C (248 μA cm^{-2}_{Pt} and 0.21 $m^2\ g^{-1}_{Pt}$, respectively). It is interesting to note that the experimental test for $PtFe_{high}Cu_{low}$ show outstanding performance of onset potential and catalytic activities, i.e., specific and mass activities, for ORR, confirming that added Cu to a binary PtFe

nanoparticle plays an important role for enhancing the catalytic function. While the PtFe and $PtFe_{low}Cu_{high}$ exhibit comparable mass activity, the specific activity of $PtFe_{low}Cu_{high}$ is much higher than PtFe. The difference in ORR performance between theoretical prediction and the experimental results is attributed to the different ECSAs and the slightly smaller size of the synthesized PtFe nanoparticles: the particle diameter of the synthesized PtFe catalysts was approximately 0.3 nm smaller than that of the PtFeCu catalysts.

Figure 4 shows that the enhanced activity of the ternary alloys was proven by both computational and the experimental results. However, it is difficult to use these alloys in practical and commercial applications without the assurance of long-term stability. Accordingly, we evaluated the stability of the ternary alloy nanoparticles. The electrochemical dissolution potentials were computed for the model nanoparticles, and their values for PtFe, $PtFe_{high}Cu_{low}$, and $PtFe_{low}Cu_{high}$ with identical particle size are 0.96, 0.93, and 0.91 V, respectively, as described in Figure S7. The binary (PtFe) and ternary (PtFeCu) nanoparticles were estimated to have higher dissolution potentials than pure, 2.0 nm nanoparticles of Pt (0.83 V versus standard hydrogen electrode [SHE]). It is interesting to note that the PtFe binary catalyst has the highest electrochemical stability.

The durability of alloy nanocatalysts is not governed only by their electrochemical environments because catalysts inevitably undergo chemical reactions on their surface. In fact, there are many reports that 3d transition metals, such as Fe and Cu, can be segregated easily by their abilities to adsorb oxygen.[41–43] Hence, it is necessary to determine whether the surface structures maintain their structural integrity during the adsorption of oxygenate intermediates during ORR.

To investigate the surface segregation induced by the oxygen adsorbate, we set up a passivation model in which it was assumed that oxygen is poisoned at the edge or vertex sites of a nanoparticle due to their strong oxygen binding.[44–46] The segregations of alloying elements (Fe and Cu) into four surface sites ([111], edge([111] × [111]), edge([111] × [100]), and [100]) were inspected for PtFe binary nanoparticles and PtFeCu ternary nanoparticles. The following order indicates the difficulty of surface segregation, [100] > [111] > edge([111] × [100]) > edge([111] × [111]), as shown in Figure 5A. The [100] and [111] facets have stronger resistance against surface segregation than edge([111] × [100]) and edge([111] × [111]). It is meaningful in that the [111] facets are both active for ORR and resistive to the surface segregation of alloying components.

Overall, in the PtFeCu nanoparticle Fe has higher tendency to segregate into the surface than Cu. The Fe segregation energies of $PtFe_{high}Cu_{low}$ and $PtFe_{low}Cu_{high}$ into the [111] facet are −1.07 and −0.96 eV, respectively, while the Cu segregation energies are −0.46 and −0.58 eV, i.e., approximately half of the affinities of Fe. The relatively low surface segregation energies of Cu atoms also have been observed in other sites, as indicated in Figure 5A. This implies that the high composition of Cu in the PtFeCu ternary alloy can improve chemical stability since Cu replaces Fe in the subshell. However, the Cu concentration is limited in the $PtFe_{low}Cu_{high}$ ($Pt_{0.8}Fe_{0.08}Cu_{0.12}$) because, as the Cu composition increases, Cu atoms easily can be located at the outmost surface sites in the ternary catalyst. It can be inferred from the results that the structure of the Pt skin can be destroyed by the high content of Cu due to the Cu in the surface and its de-alloying process (Figures 2A and S9).

The distribution of the alloying elements was analyzed further to infer the stability of PtFeCu with different compositions (Figure 5B). Previous studies have demonstrated

that the existence of different elements in the first shell is critical in the degradation of the catalysts.[24] Since it was also determined that the sub-surface elements can be segregated into the outermost shell, the elemental distributions in first and second shells were computed. The atomic fraction was averaged with 10 randomly generated initial configurations of 3.0 nm nanoparticles from 9,000 MC step simulations. As the Cu content increases, the Fe compositions of both the first and second shells decrease. These results also indicate that the introduction of Cu can enhance the catalytic stability. It is expected that Cu in the outermost shell is likely to be de-alloyed and accordingly, the $PtFe_{low}Cu_{high}$ nanoparticles with low Fe contents in their first and second shells will be resistive over electrochemical cycles.

The improvement of durability by the formation of ternary alloys was also demonstrated by the experimental durability tests. An accelerated stress test (AST) suggested by US DOE was conducted by using square wave potential cycling of 0.6 V for 3 s and 0.95 V for 3 s. Figures 5C, 5D, and S11 compare the catalytic activities, i.e., specific activity and mass activity, and ECSA at 0.9 V before and after AST for 30,000 (30k), respectively. It was confirmed that the Pt/C and PtFe catalysts have similar durabilities. From the TEM images in Figure S8, we found that the large drop (−42.1%) of ECSA in PtFe is due to the growth of the particles (from 2.95 to 4.56 nm) during the AST 30k. However, both PtFeCu catalysts increased in size by only 0.3 nm during the experiments. Besides, we observed that the variations of $\Delta E_{1/2}$ after AST 30k were 17 mV for PtFe, only 4 mV for $PtFe_{high}Cu_{low}$, and −4 mV for $PtFe_{low}Cu_{high}$ (Figure S10). The results indicate that the addition of Cu enhances the durability of the PtFe catalyst. In addition, the specific activity and mass activity values of the $PtFe_{high}Cu_{low}$ samples were three times higher than that of Pt/C (Figures 5C and 5D), and their mass activity exceeded the US DOE's 2020 target (0.44 A mg^{-1}_{Pt}) before and even after the AST 30k.

In this study, a systematic investigation of the previously reported beneficial roles of Cu was conducted, including the modulation of the strain energy of the surface Pt and the prevention of the segregation of Fe into the active surfaces of the catalyst. Furthermore, the machine-learning-driven, configurational-space searching algorithm enabled the optimization of the alloy ratio of PtFeCu. $PtFe_{low}Cu_{high}$ exhibited the best catalytic performance among the samples of ternary composition. Our results for the catalytic performance of $PtFe_{low}Cu_{high}$ are comparable with those of the previously reported PtFe binary and ternary nanocatalysts for ORR (Table S3).

EXPERIMENTAL PROCEDURES

Resource availability

Lead contact

Further information and requests for resources and reagents should be informed to and will be fulfilled by the lead contact, Byungchan Han (bchan@yonsei.ac.kr).

Materials availability

This study did not generate any new unique reagent or material.

Data and code availability

All data supporting this study are available in the manuscript and supplemental information.

Computational details

We utilized Kohn-Sham DFT calculations as implemented in the Vienna ab-initio Simulation Package.[47,48] We used projector-augmented wave pseudo-potentials for the interaction between the core and electrons.[49] All Kohn-Sham DFT equations

were calculated with the energy and force convergences of 10^{-5} eV and 0.05 eV $Å^{-1}$, respectively, and the basis plane waves were expanded with a cutoff energy of 520 eV. The exchange-correlation functional was described by the generalized gradient approximation of Perdew-Burke-Ernzerhof (PBE)[50] and revised PBE.[51] The spin polarization and van der Waals (vdW) interaction with the DFT-D3 method by Grimme et al.[52] were considered, and the magnetism of PtFeCu was obtained by initializing the different magnetic moments of Fe. The Γ-point scheme was used for the nanoparticle calculations, and a vacuum space of 10 Å was guaranteed to neglect the interaction between the periodic images. The configurations and compositions of the nanoparticles were randomly generated with compressed lattice parameters from the bulk (0.975 bulk lattice) to incorporate the compressive effect on nanoparticle optimization in a vacuum.[53] Each nanoparticle for the first-principle database was calculated with a single point.

The adsorption energy (E_{ads}) of an adsorbate was calculated as shown in Equation 1,

$$E_{ads} = E_{NP+adsorbate} - E_{NP} - E_{adsorbate}, \quad \text{(Equation 1)}$$

where $E_{NP\ +\ adsorbate}$, E_{NP}, and $E_{adsorbate}$ are the total energy of a nanoparticle with adsorbate, a nanoparticle, and an adsorbate, respectively. The free energy (ΔG) in ORR was calculated with Equation 2, as previously proposed[54] to identify the thermodynamic potential for the spontaneous ORR reaction.

$$\Delta G = \Delta E + \Delta ZPE - T\Delta S - neU, \quad \text{(Equation 2)}$$

where ΔE is the change in the internal energy of the reaction obtained by the DFT calculations. ΔZPE and ΔS are the changes in the zero-point energy and the vibrational entropy, respectively. U is an electrode potential referenced to the standard hydrogen electrode, and n is the number of electrons participating in the reaction. The free energy diagram was plotted at pH 0 and the associative ORR mechanism was considered (Equations 3, 4, 5, and 6):

$$* + O_2 + H^+ + e^- \rightarrow *OOH, \quad \text{(Equation 3)}$$

$$*OOH + H^+ + e^- \rightarrow * O + H_2O, \quad \text{(Equation 4)}$$

$$*O + H^+ + e^- \rightarrow * OH, \quad \text{(Equation 5)}$$

$$*OH + H^+ + e^- \rightarrow * + H_2O. \quad \text{(Equation 6)}$$

The reaction free energy of ORR was calculated from the experimental value[54] of the following reaction, $O_2 + 2H_2 \rightarrow 2H_2O$, $\Delta G = -4.92$ eV at 298.15 K and 0.035 bar. All oxygenate intermediates were adsorbed on the (111) surface of our model nanoparticles, which were passivated by oxygen at the edges and vertexes, as was done in previous studies.[46,55] The adsorption sites were selected as the sites that appeared most frequently in the surface (Figure S6).

The NNP was constructed with an atomistic machine-learning package (AMP)[56] interfaced with atomistic simulation environment.[57] The Gaussian descriptors of radial and angular symmetry functions (G^2 and G^4) proposed by Behler and Parrinello[25] were employed. The local symmetries were considered within the range of 5 Å. With various parameters set of G^2 and G^4, a total of 108 symmetry functions as a unique vector for each atomic species was used for the input layer of the neural network. The activation function between the hidden layers was a hyperbolic tangent, and the potential was trained until the RMSE was less than 1 meV $atom^{-1}$ with the Broyden-Fletcher-Goldfarb-Shanno algorithm.[58–60] Other hyperparameters

of the number of nodes and hidden layers were tested with 40-30-20-10 and 15-15 to efficiently train potentials while preserving the test RMSE of 10 meV atom^{-1}.

To search thermodynamically stable configurations as a function of alloy composition, we performed Monte Carlo simulations in a grand canonical ensemble scheme. Each Monte Carlo step was composed of *N* attempts of interchanging atomic positions, which were selected randomly according to Metropolis's algorithm.[34,61] All simulations were conducted until the trial attempts reached 10,000 at *T* is close to zero Kelvin neglecting any thermal effect.

The surface segregation energy (E_{seg}) of the alloy component induced by the adsorption of atomic oxygen was calculated to evaluate the chemical stability of the ternary PtFeCu nanoparticles, as shown in Equation 7:

$$E_{seg} = E(Pt_mFe_nCu_l)_{seg} - E(Pt_mFe_nCu_l)_{initial}, \quad \text{(Equation 7)}$$

where $E(Pt_mFe_nCu_l)_{seg}$ and $E(Pt_mFe_nCu_l)_{initial}$ are total energy of $Pt_mFe_nCu_l$ with and without surface segregation, respectively. *m*, *n*, and *l* are the total atom numbers of Pt, Fe, and Cu, respectively, in the ternary PtFeCu nanoparticle. Herein, the lower segregation energy is the easier segregation occurs.

Synthesis of the PtFeCu

The PtFe catalyst was synthesized by a simple, ultrasound-assisted, polyol method. First, 2.6 mmol of $Pt(acac)_2$, 3.9 mmol of $Fe(acac)_3$, and 1.35 g of thermally graphitized Ketjen black 600J (at 1,200°C) were dispersed in 100 mL of Ar-purged ethylene glycol (EG). This precursor dispersion was irradiated with a solid, horn-type sonicator (Sonics & Materials, VCX-750, tip diameter: 13 mm; amp. 40%). During the ultrasonic reaction for 4 h, the temperature was maintained above 150°C. Then, the dark slurry was sieved with a membrane filter (Advantec Toyo Kaisha, 0.4 μm pore size). To remove the residue and EG, we washed the sample several times with excess ethanol and deionized (DI) water. The sample flake that was obtained was dried overnight in an oven at 80°C overnight. Then, the as-prepared sample was placed in an alumina crucible followed by annealing at 400°C in a mixture of H_2/Ar (v/v % = 4/96) for 2 h. To remove any undesirable residues, such as FeO_x, from the annealed sample, the sample was dispersed in mixed ethanol and 0.1 M $HClO_4$ (v/v % = 1/4) followed by acidic treatment twice at 94°C over a period of 2 h. The ternary PtFeCu catalysts were synthesized by the same procedure, except for the composition and ratio of the metal precursors. All samples were synthesized at 2 g per batch.

Characterization

The crystal structure was characterized using an X-ray diffractometer (XRD, Bruker D2 Phaser XE, Cu Kα, λ = 1.5406 Å). The elemental composition and Pt loading of the sample were calculated by averaging the values measured using an elemental analyzer (FlashEA 1112, Thermo Finnigan) and inductively coupled plasma atomic emission spectroscopy (ICP-AES, Optima 4300 DV). The Pt loading in the catalyst film on a rotating disk electrode (RDE) was evaluated using an X-ray fluorescence analyzer (HORIBA, MESA-50). Particle size and the distribution of alloying elements in the sample were obtained using field emission TEM (FE-TEM) (FEI, Talos F200X, 200 kV) and Cs-corrected FE-TEM (FEI, Titan cubed G2 60-300, 300 kV).

Electrochemical measurements

A sample of 10 mg of powder was dispersed in 10 mL of solution mixed with DI water and isopropyl alcohol (v/v % = 4:1). Ionomer dispersion (FSS-2, Asahi Glass) of 10 μL was added to the catalyst dispersion and sonicated using a bath-type device until a

uniform catalyst ink was formed. Then, 13.3 μL of the catalyst ink was placed on the glassy carbon RDE (5.0 mm disk OD; 12.0 mm OD PTFE shroud; active area, 0.196 cm^2; Pine Research Instrumentation). The Pt loading on the glassy carbon was fixed at 20.4 μg cm^{-2}. Electrochemical measurements were conducted using a three-electrode cell system that consisted of catalyst-coated RDE as a working electrode, an RHE (Gaskatel) as a reference electrode, and Pt wire as a counter electrode. Before any measurements were made, the catalyst-coated RDE was cleaned by 300 cyclings of the potential over the range from 0.03 to 1.1 V (versus RHE) in N_2-saturated 0.1 M $HClO_4$. The CVs of each sample was recorded at a scan rate of 20 mV s^{-1} in the solution. An LSV of each sample for ORR was recorded at a scan rate of 10 mV s^{-1} and 1,600 rpm in the potential range from 0.0 to 1.1 V (versus RHE) in O_2-saturated 0.1 M $HClO_4$. The LSV curve was also recorded to remove the background current under the same condition except for the N_2-saturated solution of 0.1 M $HClO_4$. IR-compensation was also conducted by impedance measured at 0.7, 0.8, and 0.9 V during the ORR catalysis. The AST was conducted by applying square wave potential cycles between 0.6 V (3s) and 0.95 V (3s) for 30k in accordance with the US DOE protocol for the electrocatalyst.

Conclusions

We demonstrated the catalytic properties of PtFeCu nanocatalysts for ORR by using a machine-learning-driven configurational searching algorithm of NNP for first-principle calculations. It was successfully applied to identify the ground-state structure from calculated ternary nanoparticle phase diagram. More interestingly, we unveiled the most promising compositions of the alloying components with underlying mechanism and key descriptor of the catalytic performance. To validate the computational outcomes, ternary PtFeCu nanoparticles were experimentally designed with 2 g per batch production capacity, which is close to commercial-grade production. Four nanoparticles with varying alloying compositions (Pt, PtFe, $PtFe_{high}Cu_{low}$, and $PtFe_{low}Cu_{high}$) were successfully fabricated in accordance with our computational phase diagram for the ternary nanoparticles. Experimental measurements for electrocatalytic performance of $PtFe_{high}Cu_{low}$ for ORR activity and the durability exceeded the US DOE 2020 target even after prolonged accelerated tests. Both our computational and experimental studies posited that the underlying mechanism of high catalytic performance is the fact that Cu plays a key role for regulating surface strain distribution and segregation of Fe atoms. In particular, the $PtFe_{high}Cu_{low}$ nanoparticles had an ideal strain due to Fe and Cu in the second shell of the nanoparticle. Our computational predictions were substantiated consistently by the experimental measurements. Our strategy of interlocking the theoretical approach with experimental validation can be promising for overcoming the materials size and the component gaps to develop highly functional electrocatalysts far beyond the conventional pure Pt or binary PtM catalysts.

SUPPLEMENTAL INFORMATION

Supplemental information can be found online at https://doi.org/10.1016/j.checat.2021.06.001.

ACKNOWLEDGMENTS

This work is funded by the Global Frontier Program through the Global Frontier Hybrid Interface Materials (GFHIM) of the National Research Foundation of Korea (NRF) funded by the Ministry of Science and ICT (project no. 2013M3A6B1078882) and the R&D Collaboration Programs of Hyundai Motor Company.

AUTHOR CONTRIBUTIONS

H.C. and E.L. contributed equally to this work. H.C., S.H.N., and B.H. planned the research. H.C., K.N., and S.H.N. designed and performed the simulations. E.L. designed and performed the experiments. H.C., E.L., S.H.N., and B.H. wrote the manuscript. H.C., E.L., K.N., J.-H.J., W.K., S.H.N., and B.H. analyzed the data. S.H.N. and B.H. supervised the research.

DECLARATIOION OF INTERESTS

A Korea patent application based on the technology described in this was granted to S.H.N., B.C., and H.C. (patent no. KR 10-2021-0037961). The other authors declare no competing interests.

Received: April 8, 2021
Revised: May 12, 2021
Accepted: June 3, 2021
Published: June 28, 2021

REFERENCES

1. Cano, Z.P., Banham, D., Ye, S., Hintennach, A., Lu, J., Fowler, M., and Chen, Z. (2018). Batteries and fuel cells for emerging electric vehicle markets. Nat. Energy *3*, 279–289.
2. Guarnieri, M. (2012). Looking Back to Electric Cars (IEEE)), pp. 1–6.
3. Pivovar, B. (2019). Catalysts for fuel cell transportation and hydrogen related uses. Nat. Catal. *2*, 562–565.
4. Tripković, V., Skúlason, E., Siahrostami, S., Nørskov, J.K., and Rossmeisl, J. (2010). The oxygen reduction reaction mechanism on Pt(111) from density functional theory calculations. Electrochim. Acta *55*, 7975–7981.
5. Debe, M.K. (2012). Electrocatalyst approaches and challenges for automotive fuel cells. Nature *486*, 43–51.
6. Holton, O.T., and Stevenson, J.W. (2013). The role of platinum in proton exchange membrane fuel cells. Platinum Met. Rev. *57*, 259–271.
7. Greeley, J., Stephens, I., Bondarenko, A., Johansson, T.P., Hansen, H.A., Jaramillo, T., Rossmeisl, J., Chorkendorff, I., and Nørskov, J.K. (2009). Alloys of platinum and early transition metals as oxygen reduction electrocatalysts. Nat. Chem. *1*, 552–556.
8. Bing, Y., Liu, H., Zhang, L., Ghosh, D., and Zhang, J. (2010). Nanostructured Pt-alloy electrocatalysts for PEM fuel cell oxygen reduction reaction. Chem. Soc. Rev. *39*, 2184–2202.
9. Stamenkovic, V.R., Fowler, B., Mun, B.S., Wang, G., Ross, P.N., Lucas, C.A., and Marković, N.M. (2007). Improved oxygen reduction activity on Pt3Ni(111) via increased surface site availability. Science *315*, 493–497.
10. Gong, M.X., Zhu, J., Liu, M.J., Liu, P.F., Deng, Z.P., Shen, T., Zhao, T.H., Lin, R.Q., Lu, Y., Yang, S.Z., et al. (2019). Optimizing PtFe intermetallics for oxygen reduction reaction: from DFT screening to in situ XAFS characterization. Nanoscale *11*, 20301–20306.
11. Oezaslan, M., Hasche, F., and Strasser, P. (2012). $PtCu_3$, PtCu and Pt_3Cu alloy nanoparticle electrocatalysts for oxygen reduction reaction in alkaline and acidic media. J. Electrochem. Soc. *159*, B444–B454.
12. Lim, B., Jiang, M., Camargo, P.H., Cho, E.C., Tao, J., Lu, X., Zhu, Y., and Xia, Y. (2009). Pd-Pt bimetallic nanodendrites with high activity for oxygen reduction. Science *324*, 1302–1305.
13. Chung, D.Y., Jun, S.W., Yoon, G., Kwon, S.G., Shin, D.Y., Seo, P., Yoo, J.M., Shin, H., Chung, Y.-H., and Kim, H. (2015). Highly durable and active PtFe nanocatalyst for electrochemical oxygen reduction reaction. J. Am. Chem. Soc. *137*, 15478–15485.
14. Yu, P., Pemberton, M., and Plasse, P. (2005). PtCo/C cathode catalyst for improved durability in PEMFCs. J. Power Sources *144*, 11–20.
15. Cui, C., Gan, L., Heggen, M., Rudi, S., and Strasser, P. (2013). Compositional segregation in shaped Pt alloy nanoparticles and their structural behaviour during electrocatalysis. Nat. Mater. *12*, 765–771.
16. Luo, M., Sun, Y., Zhang, X., Qin, Y., Li, M., Li, Y., Li, C., Yang, Y., Wang, L., and Gao, P. (2018). Stable high-index faceted Pt skin on zigzag-like PtFe nanowires enhances oxygen reduction catalysis. Adv. Mater. *30*, 1705515.
17. Noh, S.H., Seo, M.H., Seo, J.K., Fischer, P., and Han, B. (2013). First principles computational study on the electrochemical stability of Pt-Co nanocatalysts. Nanoscale *5*, 8625–8633.
18. Hwang, S.J., Yoo, S.J., Jang, S., Lim, T.-H., Hong, S.A., and Kim, S.-K. (2011). Ternary Pt-Fe-Co alloy electrocatalysts prepared by electrodeposition: elucidating the roles of Fe and Co in the oxygen reduction reaction. J. Phys. Chem. C *115*, 2483–2488.
19. Arumugam, B., Kakade, B.A., Tamaki, T., Arao, M., Imai, H., and Yamaguchi, T. (2014). Enhanced activity and durability for the electroreduction of oxygen at a chemically ordered intermetallic PtFeCo catalyst. RSC Adv. *4*, 27510–27517.
20. Zhao, Z., Feng, M., Zhou, J., Liu, Z., Li, M., Fan, Z., Tsen, O., Miao, J., Duan, X., and Huang, Y. (2016). Composition tunable ternary Pt-Ni-Co octahedra for optimized oxygen reduction activity. Chem. Commun. *52*, 11215–11218.
21. Zhang, C., Sandorf, W., and Peng, Z. (2015). Octahedral Pt_2CuNi uniform alloy nanoparticle catalyst with high activity and promising stability for oxygen reduction reaction. ACS Catal. *5*, 2296–2300.
22. Arumugam, B., Tamaki, T., and Yamaguchi, T. (2015). Beneficial role of copper in the enhancement of durability of ordered intermetallic PtFeCu catalyst for electrocatalytic oxygen reduction. ACS Appl. Mater. Interfaces *7*, 16311–16321.
23. Zhang, S., Zhang, X., Jiang, G., Zhu, H., Guo, S., Su, D., Lu, G., and Sun, S. (2014). Tuning nanoparticle structure and surface strain for catalysis optimization. J. Am. Chem. Soc. *136*, 7734–7739.
24. Cao, L., Zhao, Z., Liu, Z., Gao, W., Dai, S., Gha, J., Xue, W., Sun, H., Duan, X., and Pan, X. (2019). Differential surface elemental distribution leads to significantly enhanced stability of PtNi-based ORR catalysts. Matter *1*, 1567–1580.
25. Behler, J., and Parrinello, M. (2007). Generalized neural-network representation of high-dimensional potential-energy surfaces. Phys. Rev. Lett. *98*, 146401.
26. Behler, J. (2011). Atom-centered symmetry functions for constructing high-dimensional neural network potentials. J. Chem. Phys. *134*, 074106.
27. Bartók, A.P., Payne, M.C., Kondor, R., and Csányi, G. (2010). Gaussian approximation potentials: the accuracy of quantum mechanics, without the electrons. Phys. Rev. Lett. *104*, 136403.
28. Jung, H., Stocker, S., Kunkel, C., Oberhofer, H., Han, B., Reuter, K., et al. (2020). Size-extensive

molecular machine learning with global representations. ChemSystemsChem *2*, 1–7. https://doi.org/10.1002/syst.201900052.

29. Vandermause, J., Torrisi, S.B., Batzner, S., Xie, Y., Sun, L., Kolpak, A.M., and Kozinsky, B. (2020). On-the-fly active learning of interpretable Bayesian force fields for atomistic rare events. npj Comput. Mater. *6*, 1–11.

30. Paleico, M.L., and Behler, J. (2020). Global optimization of copper clusters at the ZnO(1010) surface using a DFT-based neural network potential and genetic algorithms. J. Chem. Phys. *153*, 054704.

31. Eckhoff, M., Lausch, K.N., Blöchl, P.E., and Behler, J. (2020). Predicting oxidation and spin states by high-dimensional neural networks: applications to lithium manganese oxide spinels. J. Chem. Phys. *153*, 164107.

32. Eckhoff, M., and Behler, J.r. (2019). From molecular fragments to the bulk: development of a neural network potential for MOF-5. J. Chem. Theor. Comput. *15*, 3793–3809.

33. Artrith, N., and Kolpak, A.M. (2015). Grand canonical molecular dynamics simulations of Cu-Au nanoalloys in thermal equilibrium using reactive ANN potentials. Comput. Mater. Sci. *110*, 20–28.

34. Kang, J., Noh, S.H., Hwang, J., Chun, H., Kim, H., and Han, B. (2018). First-principles database driven computational neural network approach to the discovery of active ternary nanocatalysts for oxygen reduction reaction. Phys. Chem. Chem. Phys. *20*, 24539–24544.

35. Wang, C., Chi, M., Li, D., Strmcnik, D., Van der Vliet, D., Wang, G., Komanicky, V., Chang, K.-C., Paulikas, A.P., and Tripkovic, D. (2011). Design and synthesis of bimetallic electrocatalyst with multilayered Pt-skin surfaces. J. Am. Chem. Soc. *133*, 14396–14403.

36. Lee, E., Kim, S., Jang, J.-H., Park, H.-U., Matin, M.A., Kim, Y.-T., and Kwon, Y.-U. (2015). Effects of particle proximity and composition of Pt-M (M = Mn, Fe, Co) nanoparticles on electrocatalysis in methanol oxidation reaction. J. Power Sources *294*, 75–81.

37. Zhu, J., Xiao, M., Li, K., Liu, C., and Xing, W. (2015). Superior electrocatalytic activity from nanodendritic structure consisting of a PtFe bimetallic core and Pt shell. Chem. Commun. *51*, 3215–3218.

38. Su, L., Shrestha, S., Zhang, Z., Mustain, W., and Lei, Y. (2013). Platinum-copper nanotube electrocatalyst with enhanced activity and durability for oxygen reduction reactions. J. Mater. Chem. A *1*, 12293–12301.

39. Oezaslan, M., Hasché, F., and Strasser, P. (2012). $PtCu_3$, PtCu and Pt_3Cu alloy nanoparticle electrocatalysts for oxygen reduction reaction in alkaline and acidic media. J. Electrochem. Soc. *159*, B444.

40. Li, W., and Lane, A.M. (2011). Resolving the HUPD and HOPD by DEMS to determine the ECSA of Pt electrodes in PEM fuel cells. Electrochem. Commun. *13*, 913–916.

41. Prabhudev, S., Bugnet, M., Zhu, G.-Z., Bock, C., and Botton, G.A. (2015). Surface segregation of Fe in Pt-Fe alloy nanoparticles: its precedence and effect on the ordered-phase evolution during thermal annealing. ChemCatChem *7*, 3655.

42. Noh, S.H., Han, B., and Ohsaka, T. (2015). First-principles computational study of highly stable and active ternary PtCuNi nanocatalyst for oxygen reduction reaction. Nano Res. *8*, 3394–3403.

43. Escaño, M.C.S., and Kasai, H. (2014). First-principles study on surface structure, thickness and composition dependence of the stability of Pt-skin/Pt_3Co oxygen-reduction-reaction catalysts. J. Power Sources *247*, 562–571.

44. Kirchhoff, B., Braunwarth, L., Jung, C., Jónsson, H., Fantauzzi, D., and Jacob, T. (2020). Simulations of the oxidation and degradation of platinum electrocatalysts. Small *16*, 1905159.

45. Hu, J., Wu, L., Kuttiyiel, K.A., Goodman, K.R., Zhang, C., Zhu, Y., Vukmirovic, M.B., White, M.G., Sasaki, K., and Adzic, R.R. (2016). Increasing stability and activity of core-shell catalysts by preferential segregation of oxide on edges and vertexes: oxygen reduction on Ti-Au@ Pt/C. J. Am. Chem. Soc. *138*, 9294–9300.

46. Jinnouchi, R., Suzuki, K.K.T., and Morimoto, Y. (2016). DFT calculations on electro-oxidations and dissolutions of Pt and Pt-Au nanoparticles. Catal. Today *262*, 100–109.

47. Kresse, G., and Furthmüller, J. (1996). Efficient iterative schemes for ab initio total-energy calculations using a plane-wave basis set. Phys. Rev. B *54*, 11169.

48. Hafner, J. (2008). Ab-initio simulations of materials using VASP: density-functional theory and beyond. J. Comput. Chem. *29*, 2044–2078.

49. Blöchl, P.E. (1994). Projector augmented-wave method. Phys. Rev. B *50*, 17953.

50. Perdew, J.P., Burke, K., and Ernzerhof, M. (1996). Generalized gradient approximation made simple. Phys. Rev. Lett. *77*, 3865.

51. Hammer, B., Hansen, L.B., and Nørskov, J.K. (1999). Improved adsorption energetics within density-functional theory using revised Perdew-Burke-Ernzerhof functionals. Phys. Rev. B *59*, 7413.

52. Grimme, S., Antony, J., Ehrlich, S., and Krieg, H. (2010). A consistent and accurate ab initio parametrization of density functional dispersion correction (DFT-D) for the 94 elements H-Pu. J. Chem. Phys. *132*, 154104.

53. Huang, Z., Thomson, P., and Di, S. (2007). Lattice contractions of a nanoparticle due to the surface tension: a model of elasticity. J. Phys. Chem. Sol. *68*, 530–535.

54. Nørskov, J.K., Rossmeisl, J., Logadottir, A., Lindqvist, L., Kitchin, J.R., Bligaard, T., and Jonsson, H. (2004). Origin of the overpotential for oxygen reduction at a fuel-cell cathode. J. Phys. Chem. B *108*, 17886–17892.

55. Wei, G.-F., and Liu, Z.-P. (2013). Optimum nanoparticles for electrocatalytic oxygen reduction: the size, shape and new design. Phys. Chem. Chem. Phys. *15*, 18555–18561.

56. Khorshidi, A., and Peterson, A.A. (2016). Amp: a modular approach to machine learning in atomistic simulations. Comput. Phys. Commun. *207*, 310–324.

57. Larsen, A.H., Mortensen, J.J., Blomqvist, J., Castelli, I.E., Christensen, R., Dułak, M., Friis, J., Groves, M.N., Hammer, B., and Hargus, C. (2017). The atomic simulation environment—a Python library for working with atoms. J. Phys. Condens. Matter *29*, 273002.

58. Broyden, C.G. (1970). The convergence of a class of double-rank minimization algorithms 1. General considerations. IMA J. Appl. Math. *6*, 76–90.

59. Fletcher, R. (1970). A new approach to variable metric algorithms. Comput. J. *13*, 317–322.

60. Goldfarb, D. (1970). A family of variable-metric methods derived by variational means. Math. Comput. *24*, 23–26.

61. Han, B., Van der Ven, A., Ceder, G., and Hwang, B.-J. (2005). Surface segregation and ordering of alloy surfaces in the presence of adsorbates. Phys. Rev. B *72*, 205409.